ROTATING BLADE FLOW INSTABILITY AS A SOURCE OF NOISE IN AXIAL TURBOMACHINES

F. Kameier

BMW Rolls-Royce Aeroengines, Eschenweg, 15827 Dahlewitz, Germany

AND

W. Neise

Deutsche Forschungsanstalt für Luft- und Raumfahrt e.V., Institut für Antriebstechnik, Abteilung Turbulenzforschung Berlin, Müller-Breslau-Straße 8, 10623 Berlin, Germany

An experimental study is presented to investigate the aeroacoustic generation mechanism of the tip clearance noise in axial turbomachines. In addition to the increased broadband levels reported in the literature when the tip clearance is enlarged, significant level increases were observed within narrow frequency bands below the blade passing frequency. Measurements of the pressure fluctuations at the casing wall just upstream of the entrance plane of the impeller and on the rotating blades reveal that the tip clearance noise is associated with a rotating blade flow instability at the blade tip which in turn is only present under reversed flow conditions in the tip clearance gap. The rotating instability is interpreted as a rotating source or vortex mechanism which moves relative to the blade row at a fraction of the impeller shaft speed, similar to the cell(s) of rotating stall. A model for the generation of the narrow-band tip clearance noise is presented.

© 1997 Academic Press Limited

1. INTRODUCTION

An experimental study is described to investigate the aeroacoustic generation mechanism of the tip clearance noise in axial turbomachines. In turbomachinery it is generally understood that the tip clearance flow is driven by the pressure difference between the pressure side and the suction side of the blades and forms a vortex at the tip of each blade, which is similar to the vortex at the end of an aircraft wing. The vortices are attached to the blade tips from where they are convected downstream with the main flow; the flow field between two adjacent blades is not affected much by the presence of the vortices. It was shown by Kameier [1] and Kameier and Neise [2] that there is another secondary flow in the blade tip region, in addition to the classical tip vortex, which is produced by the pressure difference between the suction side and the pressure side of the entire impeller disk of an axial turbomachine; see the flow sketch in Figure 1. Differently from the blade tip vortex, the reversed flow condition in the blade tip regime extends over the entire circumference of the rotor, as was shown by means of hot wire measurements in the blade tip gap. The size of the radial gap between blade tip and casing wall is decisive for the strength of the secondary flow, which in turn influences the mean flow field in the tip region including the flow separation processes at the blade tips. The flow pattern can be explained as a separated boundary layer, with a separation point upstream of the rotor and a reattachment in the trailing edge region of the blade.
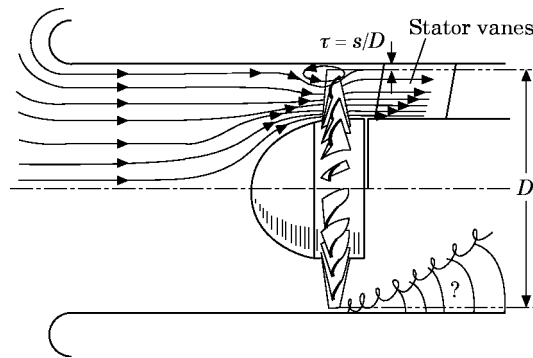
Figure 1. Schematic view of secondary flow driven by pressure difference between suction and pressure side in the tip region.

The aerodynamics of the blade tip flow have been studied extensively in the past; however, there are only very few studies dealing with tip clearance noise. Marcinowski [3] was the first to publish a paper on this topic. His results showed increases of broadband noise levels with increasing tip clearance, with the largest changes in a frequency region above the blade passing frequency. Mugridge and Morfey [4] argued that an optimum tip clearance exists at which the broadband noise is minimum due to the counteraction of the tip clearance flow with the blade passage vortex. This result was not confirmed by Longhouse [5] who searched for a practical solution of the tip clearance noise emitted by automotive cooling fans and devised a rotating impeller shroud for this application. From flow visualization studies he concluded that tip clearance noise is caused by an unsteady interaction of the blade tip vortex with the blade trailing edge and the leading edge of the following blade. As a result, the broadband noise level is increased. The lowest noise levels were obtained with the smallest possible tip clearance. Similar findings were reported by Fukano et al. [6], Stütz [7], and Cudina [8]. While in references [3–8] higher broadband levels were reported as a result of an enlarged tip clearance, drastic level increases were reported in references [1] and [2] within limited frequency regions below the blade passage frequency, in addition to the higher random noise. A turbulence generator inserted into the tip clearance gap was found to be effective in diminishing the tip clearance noise and in improving the aerodynamic performance at the same time.

The present paper is aimed at gaining a better understanding of the physical generation mechanism of the tip clearance noise. For this purpose, measurements of pressure fluctuations in the tip region of the impeller blades were performed, both in the fixed frame of reference and on the rotating impeller blades. A simple experiment involving a rotating loudspeaker in a duct helps explain the frequency components generated by a rotating aerodynamic source mechanism.

2. EXPERIMENTAL FACILITY

The test fan is a low-speed high-pressure axial fan with outlet guide vanes. The design is similar to an axial fan manufactured by J. M. Voith GmbH, Heidenheim, Germany (now Voith Howden GmbH) who kindly supplied the impeller blades. The impeller diameter was kept constant throughout all experiments, and the tip clearance was varied by changing the casing diameter: Four different casing segments were used to give gap widths of $s = 0.3$, 0.6, 1.2, and 2.4 mm which correspond to tip clearance ratios of $\tau = s/D = 0.00066$, 0.0013, 0.0027, and 0.0053. The principal impeller dimensions are as
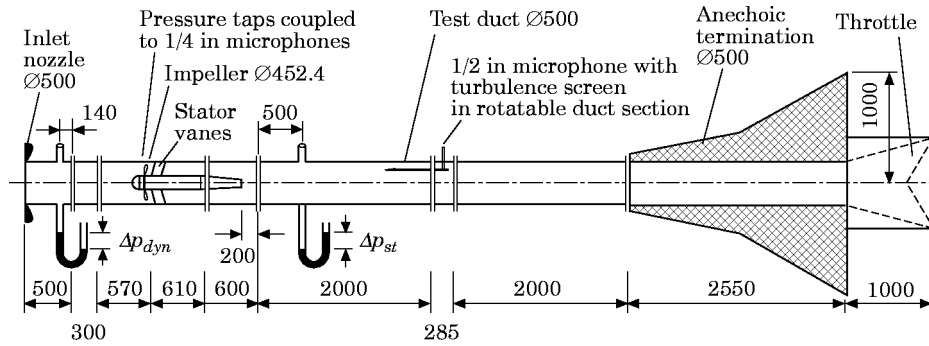
Figure 2. Experimental set-up (dimensions in mm).

follows: impeller diameter $D = 452.4$ mm; hub-to-tip ratio $\varepsilon = 0.62$; NACA 65 blade profile; blade number $Z = 24$; blade chord length at the tip $c = 43$ mm; blade stagger angle at the tip $\theta = 27°$.

The stator row comprises $V = 17$ non-profiled vanes. Figure 2 shows the experimental set-up along with its major dimensions. The measurement facility meets the requirements of DIN 24 163 [9] for measurement of the aerodynamic fan performance. On the inlet side there is a short duct section with a bellmouth nozzle; there are no flow straighteners nor screens in the inlet duct. The anechoically terminated outlet duct is in accordance with the standardized in-duct method DIN EN 25 136 [10], ISO 5136 [11]. A 1/2 in microphone equipped with a turbulence screen is mounted in a rotatable duct section to measure the circumferentially averaged sound pressure level at a specified radial distance from the duct axis. The pressure fluctuations on the interior casing wall are monitored by using 1/8 in microphones (Brüel & Kjaer type 4138) which are mounted flush with the inner wall; see Figure 3. To measure the unsteady blade pressures, four miniature pressure sensors (Kulite type LQ 47-5-SG) are mounted in small grooves of the impeller blades so that the original outer blade contour is retained; see the schematic in Figure 4. The low-voltage output signals of the sensors are amplified within the rotating system and then transmitted into the fixed frame of reference via a two-channel telemetry system (Datatel). More details about the experimental equipment and measurement techniques have been given by Kameier [1].
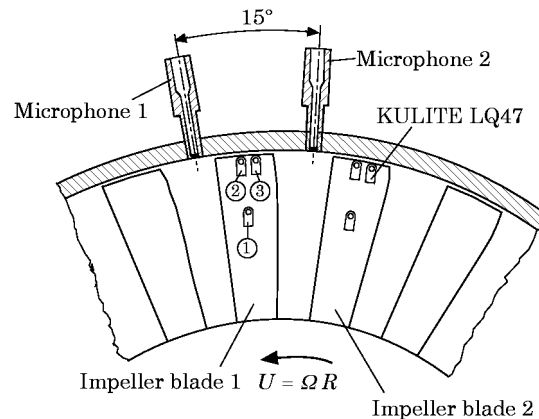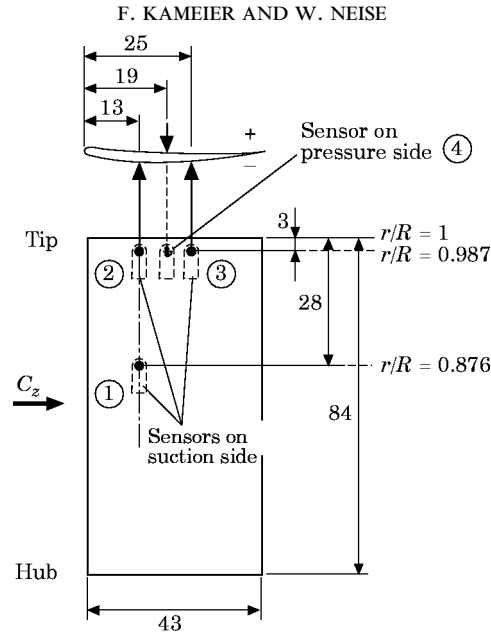

Figure 3. Sectional view of the impeller with KULITE LQ 47 mounted in the impeller blade and 1/8 in microphones B&K 4138 mounted flush with inner casing wall.

Figure 4. Schematic of pressure sensors mounted on the impeller blade. Dimensions in mm.

3. TIP CLEARANCE NOISE

In earlier papers by Marcinowski [3], Longhouse [5], Fukano *et al*. [6], and Stütz [7], increases in broadband noise were reported as the result of an enlarged tip clearance. The sound pressure spectra depicted in Figure 5, which were measured in the fan outlet duct, support this finding. The rotor speed is 1400 r.p.m. which corresponds to a rotor tip speed of $U = 33 \cdot 16$ m/s and a rotor tip Mach number of $Ma = 0 \cdot 10$. The blade passing frequency component is $BPF = 560$ Hz. According to the Tyler and Sofrin analysis [12], the azimuthal mode order m of the spinning modes generated by rotor/stator interaction is given by $m = hZ \pm vV$, where $h = 1, 2, 3, \ldots$ for the blade passing frequency component and its harmonics, and $v = 1, 2, 3, \ldots$. From this follows for the present case that the lowest azimuthal mode order of the blade passing frequency component produced by rotor/stator interaction is $m = 7$, the cut-off frequency of which in a 500 mm diameter duct is 1873 Hz under standard atmospheric conditions ($a_0 = 343$ m/s); i.e., this mode is cut-off. Since the blade passing frequency component is visible in the spectrum, though of low level, one concludes that it must be the interaction of the rotor with inlet flow distortions (non-uniformities of the intake flow and/or inflow turbulence; see the review paper by Cumpsty [13]) that causes the blade tone fundamental. The lowest azimuthal mode order of the second blade tone harmonic $2 \times BPF = 1120$ Hz is $m = -3$, the cut-off frequency of which in the fan duct is 917 Hz; hence, the rotor/stator interaction at $2 \times BPF$ contributes to the sound field in the test duct.

The bottom diagram of Figure 5 shows only the low frequency range of the spectra with enhanced frequency resolution; there it is obvious that enlarging the tip clearance results in drastic level increases of the radiated sound pressure within limited, almost narrow-band frequency regions. A particularly steep level increase of 15 dB occurs at 370 Hz when the tip clearance ratio is raised from $\tau = 0 \cdot 0027$ to $\tau = 0 \cdot 0053$.

Nawrot [14] and Kameier *et al*. [15] performed measurements with the short inlet duct shown in Figure 2 replaced by an anechoic test duct which had about the same dimensions
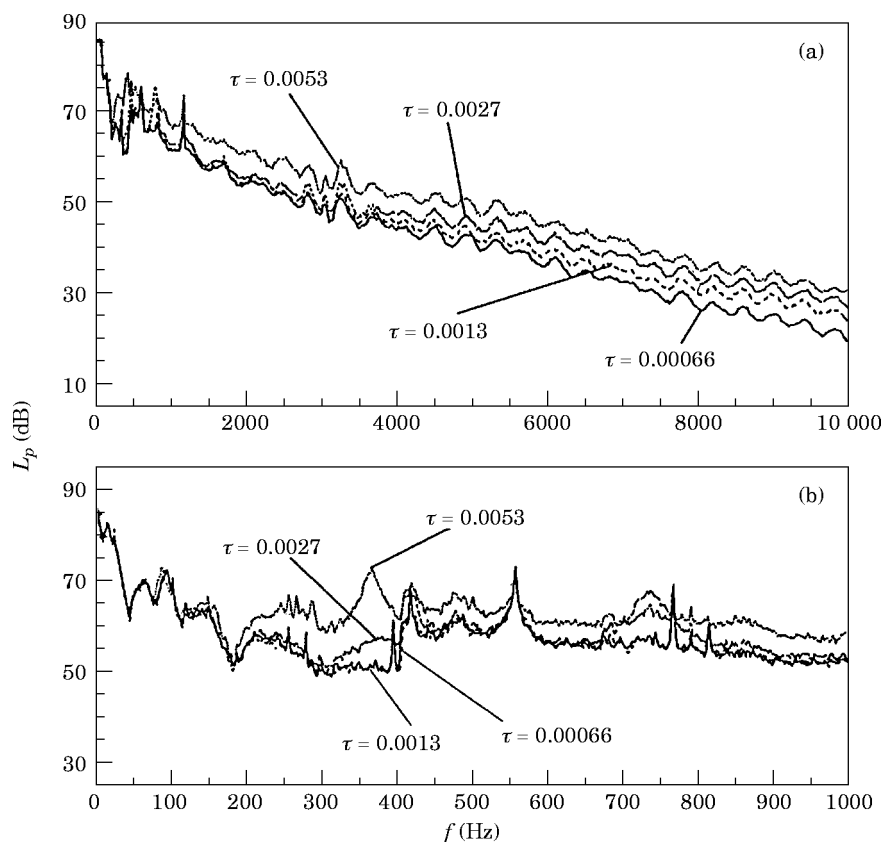
Figure 5. Sound pressure spectra in the outlet duct as a function of tip clearance, $\Phi_{opt} = 0.220$, $n = 1400$ r.p.m.; (a) frequency range 0–10 kHz, $\Delta f_B = 12.5$ Hz; (b) frequency range 0–1 kHz, $\Delta f_B = 1.56$ Hz.

as the outlet duct. The various fan performance curves measured with this arrangement were slightly different from the ones reported here, but the effect of the tip clearance was found to be unaltered. This statement holds also true for the sound spectra radiated. From these results it appears that the tip clearance effects discussed here are largely independent of the flow conditions at the fan inlet.

4. PRESSURE FLUCTUATIONS ON THE IMPELLER BLADES AND AT THE CASING WALLS NEAR THE BLADE TIPS

In Figure 6 pressure spectra are compared which were measured in the outlet duct (acoustic far field, curves labeled B) and at the casing wall at an axial location $\zeta = z/D = -0.007$ upstream of the leading edge of the impeller blades (acoustic near field, curves labeled A). The diagrams in the left column show the results for the largest tip clearance ratio ($\tau = 0.0053$) where the tip clearance noise is most prominent in the spectrum, and the right column is for the smallest tip clearance ratio ($\tau = 0.00066$). The flow coefficient Φ is reduced from the top to the bottom diagram. The outlet duct spectra represent the circumferential average of the sound pressure at a radial distance of $r = 0.65\,R$ from the duct axis. The wall pressures were measured with flush mounted 1/8 in microphones; compare Figure 3. The blade passing frequency component (*BPF*) is clearly visible in the wall pressure spectra, and multiples of the rotor frequency (*RF*) appear to both sides of this component.
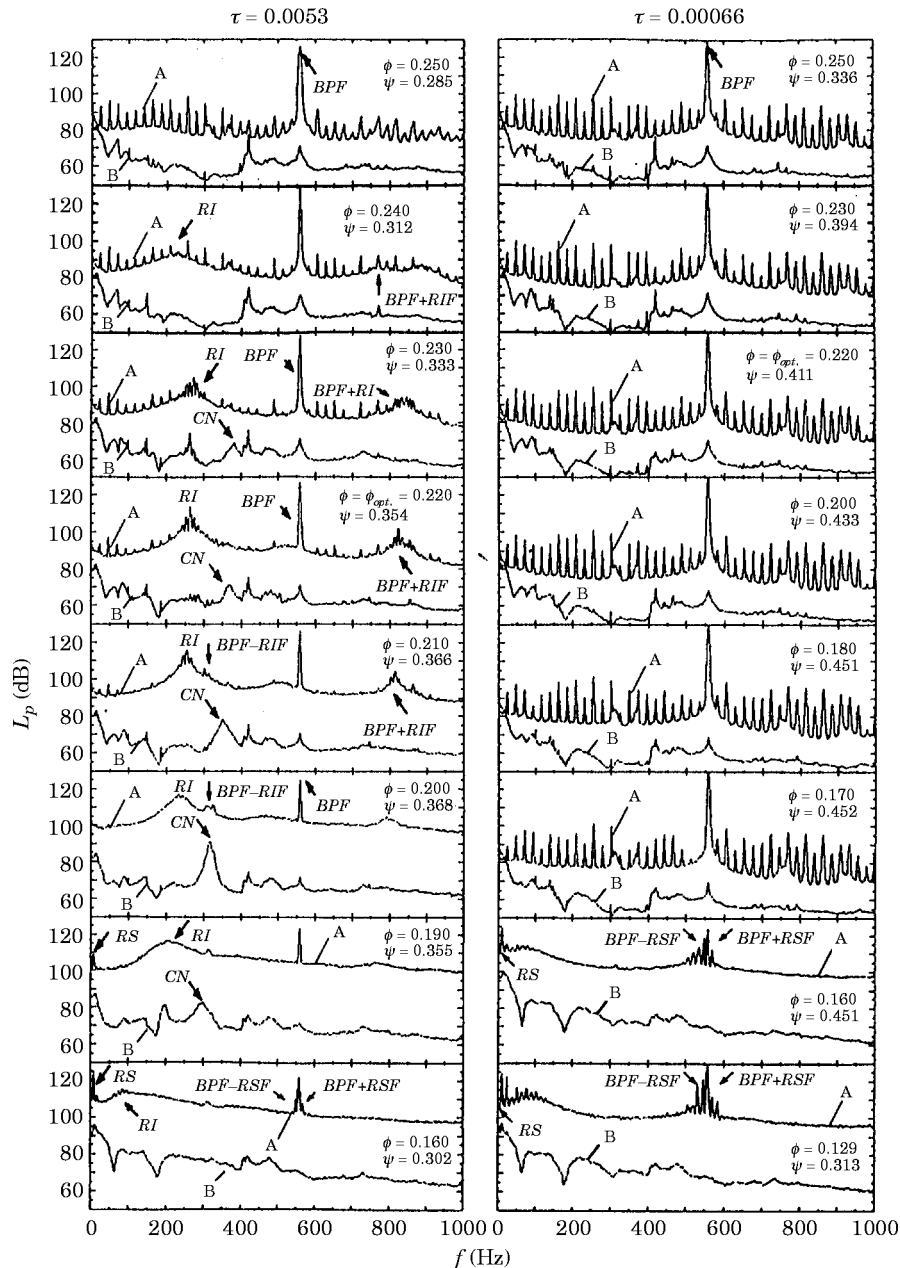
Figure 6. Pressure spectra in the outlet duct (B, far field) and at the casing wall (A, $\zeta = -0.007$, near field) for various operating conditions; $\tau = 0.0053$ (left column) and $\tau = 0.00066$ (right column); $n = 1400$ r.p.m., $\Delta f_B = 1.56$ Hz.

The tip clearance noise component (CN) measured for $\tau = 0.0053$ in the duct is shifted towards lower frequencies as the flow rate is reduced. In the wall pressure spectra another component termed rotating instability (RI) appears, which increases in level as the flow rate is throttled. At some operating conditions, tone components exist at frequencies equal to the sum or difference of the blade passing frequency and the frequency of the rotating instability component: i.e., at $BPF + RIF$ and $BPF - RIF$. At $\Phi = 0.200$ (third

diagram from the bottom) the tip clearance noise reaches its highest level. At flow rates below $\Phi = 0\cdot200$, the fan operation becomes unstable, and a tonal component below the rotor shaft frequency is generated in the outlet duct spectra as well as in the wall pressure spectra which is associated with rotating stall (RS). This also results in a frequency modulation of the blade passing frequency, and consequently side bands at $BPF + RSF$ and $BPF - RSF$ appear in the wall pressure spectrum.

With a tip clearance ratio of $\tau = 0\cdot00066$ (right column in Figure 6), the clearance noise component is missing in the spectra throughout the range of operating conditions and the rotating instability component appears together with rotating stall which in turn is observed at much lower flow rates than before: i.e., $\Phi \leqslant 0\cdot16$.

In Figure 7 are shown the pressure spectra measured on the impeller blades. The presentation is similar to that in Figure 6. The four spectra shown in each diagram correspond to the four sensor positions depicted in Figure 4. At all positions the spectra are dominated by spikes at the rotor shaft frequency and multiples thereof which indicates that the flow environment of the rotor is not quite uniform (non-uniform stator geometry, turbulent inflow distortions). Since the tone levels are highest at the rotor shaft frequency Ω and decrease monotonically with increasing frequency, it is concluded that these tones are generated by the interaction of the rotor with inlet flow distortions, compare the discussion of the origin of the blade passing frequency component in the context of Figure 5. Knowledge of the exact origin of the shaft order frequency components, however, is not of importance for the present study. For most of the flow rates tested, the "stator passing frequency" $V\Omega = 397$ Hz is not visible but buried in the random noise. When the fan is operated just near the maximum efficiency point ($\Phi = 0\cdot220$), a broadband
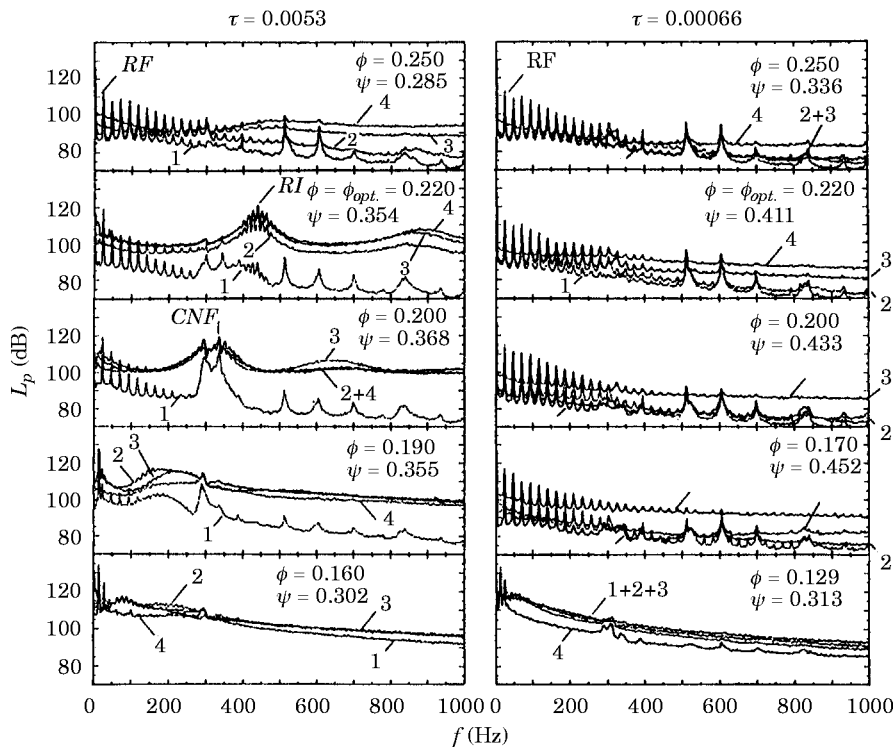

Figure 7. Spectra of the impeller blade pressures for various operating conditions; $\tau = 0\cdot0053$ (left column) and $\tau = 0\cdot00066$ (right column); $n = 1400$ r.p.m., $\Delta f_B = 1\cdot56$ Hz.

hump with superimposed multiple peaks appears in the spectrum which moves to lower frequencies when the flow is further throttled. This behavior is similar to that of the rotating instability component in the wall pressure spectra; compare Figure 6. The frequencies measured in the fixed and in the rotating frame of reference are different. Closer to the hub ($r/R = 0.876$, sensor #1), the pressure fluctuations of the rotating instability component are much lower in level than at the blade tip which reveals that the cause for this phenomenon lies in the tip flow region. Mongeau [16], Bent et al. [17], and Mongeau et al. [18] reported similar pressure spectra on the blades of a casingless centrifugal pump impeller and interpreted them as the result of a rotating "almost-frozen" discharge flow instability pattern, which rotates relative to the blades, similar to the cells of separated flow in the case of rotating stall. The term rotating flow instability is also used in the present paper; however, it will be shown in the following that the rotating instability components observed in the blade tip region of axial fans are not caused by a frozen flow disturbance but rather by a fluctuating flow disturbance, a fluctuating source mechanism which rotates relative to the blade row. The rotating flow instability components are moved to lower frequencies as the fan is throttled.

As in the case of the wall pressure spectra shown in Figure 6, the rotating instability component appears in the blade pressure spectra only at very low flow rates when the tip clearance is small; compare the diagrams in the right column of Figure 7.

With the onset of rotating stall, the low frequency random noise levels are increased, and the harmonics of the stator frequency are masked. The spectra are now dominated by the rotating stall component with the highest levels at sensor location #2 and #3: i.e., on the blade suction side at a radial distance from the axis of $r/R = 0.987$. This indicates that the blade flow is stalled first at the tip. When the flow is further reduced, the stalled flow regime extends deeper down to the hub. Note that the frequency of the rotating stall component is different from the one found in the wall pressure fluctuations (see Figure 7); the sum of the two frequencies is, of course, equal to the rotor shaft frequency.

In Figure 8 the spectra of the casing wall pressures (left column) and impeller blade pressures (right column) measured at the maximum efficiency point are compared. Also shown are in each case, the coherence γ^2 of the pressures measured at two circumferential locations spaced $\Delta\theta = 15°$ (one rotor pitch) apart and the phase angle φ_{12} of the cross-spectrum of the two signals. The two impeller blade pressure signals were measured at the sensor positions #2 on adjacent blades. Clearly, the frequencies of the rotating instability component are different in the fixed and the moving frames of reference and, also, the frequency spacing of the spikes superimposed on the broad humps. The coherence of the pressure field is large at the blade passing frequency, as was to be expected, and in the frequency range related to the rotating instability components. Note that in this range there is an almost linear variation of the phase angle with frequency, with a positive gradient in the fixed and a negative gradient in the moving frame of reference. In the following section theoretical considerations are presented to help explain the frequency characteristics of the rotating instability components as observed in the two co-ordinate systems.

5. ANALYSIS OF THE SPECTRAL COMPONENTS GENERATED BY A ROTATING SOURCE MECHANISM

5.1. THEORETICAL CONSIDERATIONS

Consider an aerodynamic source Q (subscript Q) located in the plane of the impeller which rotates at an angular velocity Ω_Q^F relative to a fixed co-ordinate system, as indicated
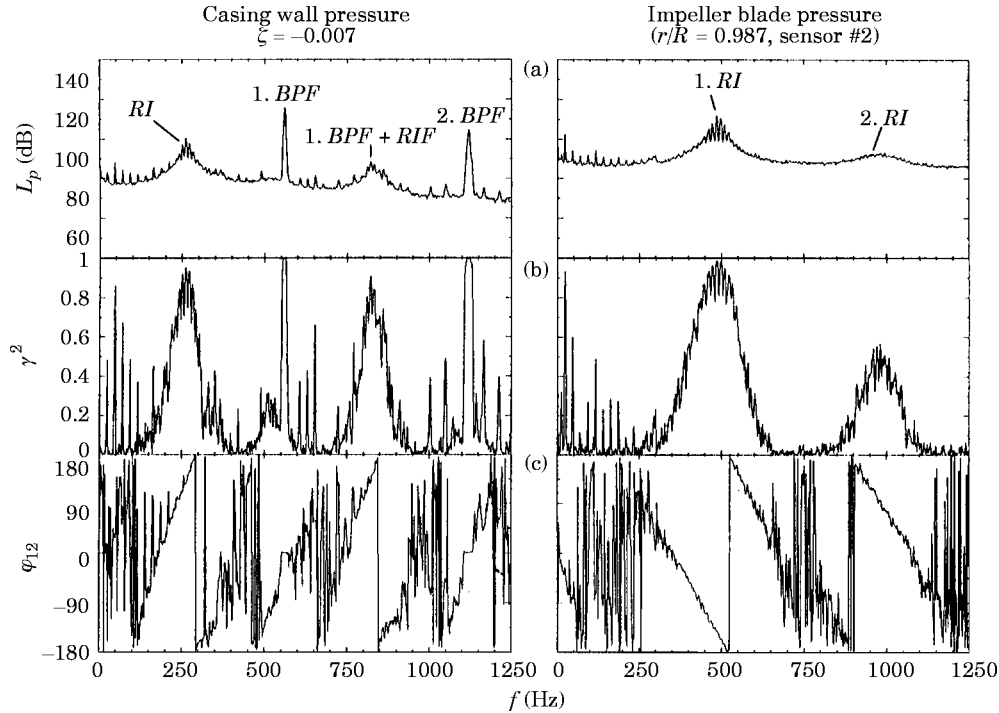
Figure 8. Comparison of the pressure fluctuations at the casing wall ($\zeta = -0.007$, left column) and on the impeller blade (sensor #2, right column); compare the arrangement shown in Figures 3 and 4; $\Phi_{opt} = 0.220$, $\tau = 0.0053$, $n = 1400$ r.p.m., $\Delta f_B = 1.56$ Hz. (a) Pressure spectra; (b) coherence; (c) phase angle of cross-spectrum.

by the superscript F. The angular co-ordinate in the fixed frame of reference is denoted θ^F; see the schematic presentation shown in Figure 9. Consider further another system of co-ordinates with an angular velocity $\Omega^F_R = \Omega$, again relative to the fixed frame of reference. In the present context, the rotating system of co-ordinates is attached to the rotating impeller. The angular velocity Ω and co-ordinate θ as measured in the rotating system of co-ordinates are denoted by the superscript R.

The azimuthal distribution of the source Q repeats after one revolution, i.e., is 2π periodic, and can therefore be represented by a Fourier series with respect to the angular co-ordinate. If the pressure field associated with the source Q is expressed in a system of co-ordinates which is moving with the source, as indicated by the superscript Q, the following relation applies:

$$p(\theta^Q, t) = \text{Re} \left\{ \sum_{\alpha = -\infty}^{\infty} A_\alpha \, e^{i(\alpha\theta^Q - \omega^Q t)} \right\}. \tag{1}$$

Equation (1) is a one-dimensional representation of pressure fluctuations associated with the source Q; θ^Q is the azimuthal co-ordinate in the reference frame of the rotating pressure field, ω^Q the angular frequency of the aerodynamic source, and A_α the amplitude of the Fourier component α. The following relations exists between the angular co-ordinates in the fixed, the rotating, and the source system,

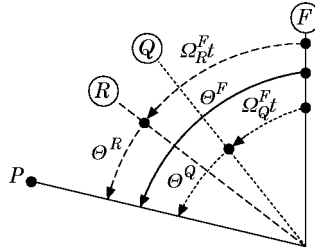$$\theta^F = \theta^R + \Omega t, \qquad \theta^F = \theta^Q + \Omega^F_Q t, \tag{2, 3}$$

Figure 9. Co-ordinate systems.

and the rotational velocities of the co-ordinate systems,

$$\Omega_Q^F = \Omega_Q^R + \Omega, \tag{4}$$

where Ω_Q^R is the angular velocity of the aerodynamic source relative to the rotating system of co-ordinates. Rearranging equations (2)–(4) yields

$$\theta^Q = \theta^F - \Omega_Q^F t, \qquad \theta^Q = \theta^R - \Omega_Q^R t. \tag{5, 6}$$

By inserting equations (5) and (6) into equation (1), one obtains

$$p(\theta^F, t) = \text{Re}\left\{ \sum_{\alpha = -\infty}^{\infty} A_\alpha \, e^{i(\alpha\theta^F - (\omega^Q + \alpha\Omega_Q^F)t)} \right\}, \tag{7}$$

$$p(\theta^R, t) = \text{Re}\left\{ \sum_{\alpha = -\infty}^{\infty} A_\alpha \, e^{i(\alpha\theta^R - (\omega^Q + \alpha\Omega_Q^R)t)} \right\}. \tag{8}$$

Equations (7) and (8) reveal that the frequency of the source as measured in the fixed and the rotating frame of reference is given by, respectively,

$$\omega^F = \omega^Q + \alpha\Omega_Q^F, \qquad \omega^R = \omega^Q + \alpha\Omega_Q^R. \tag{9, 10}$$

Only if the azimuthal source distribution is uniform, i.e., if $\alpha = 0$ is the only Fourier component present, are the frequencies measured in the fixed or the rotating system equal to the original source frequency. In all other cases, additional frequency components are generated as a result of the circumferentially non-uniform source distribution moving relative to the fixed and the rotating co-ordinate system. Equations (4), (9) and (10) can be combined to give the following relationships for the aerodynamic mode order α and the source frequency ω^Q:

$$\alpha = (\omega^F - \omega^R)/\Omega, \qquad \omega^Q = \omega^F - (\omega^F - \omega^R)\Omega_Q^F/\Omega. \tag{11, 12}$$

Equations (9) and (10) can also be used to determine the frequency generated by any Fourier component α (azimuthal mode order number of the aerodynamic source) in the fixed and the rotating system:

$$\omega_\alpha^F = \omega^Q + \alpha\Omega_Q^F, \qquad \omega_\alpha^R = \omega^Q + \alpha\Omega_Q^R, \tag{13}$$

$$\omega_{\alpha+1}^F = \omega^Q + (\alpha + 1)\Omega_Q^F, \qquad \omega_{\alpha+1}^R = \omega^Q + (\alpha + 1)\Omega_Q^R. \tag{14}$$

The angular velocity of the source mechanism relative to the fixed or the rotating frame of reference can be determined from equations (13) and (14):

$$\Omega_Q^F = \omega_{\alpha+1}^F - \omega_\alpha^F = \Delta\omega^F, \qquad \Omega_Q^R = \omega_{\alpha+1}^R - \omega_\alpha^R = \Delta\omega^R. \tag{15, 16}$$

Subtracting equation (16) from (15) yields:

$$\Omega_Q^F - \Omega_Q^R = \Omega = \Delta\omega^F - \Delta\omega^R. \tag{17}$$

If an aerodynamic source is considered with an angular velocity smaller than that of the rotating system, $\Omega_Q^F < \Omega$, then the source velocity relative to the rotating frame is negative, $\Omega_Q^R < 0$, and $\Delta\omega^R < 0$. In this case equation (17) turns into the relation

$$\Omega = |\Delta\omega^F| + |\Delta\omega^R|, \tag{18}$$

which indicates that the sum of the frequency differences between two consecutive α modes in the fixed and the rotating frame of reference is equal to the angular velocity of the rotating system.

5.2. EXPERIMENTAL DEMONSTRATION WITH A ROTATING LOUDSPEAKER IN A DUCT

To verify experimentally the above theoretical considerations, the fan test facility depicted in Figure 2 was modified in the following way. The impeller of the test fan was replaced by a flat disk of the same diameter on which a small loudspeaker was mounted; see the sketch depicted in Figure 10. The loudspeaker was fed via the hollow motor shaft and a slip ring assembly mounted at the far side of the drive motor. To monitor the pressure radiated by the loudspeaker, within the rotating system, a pressure transducer (KULITE LQ-47-5SG) together with a miniature amplifier (DLR-IAE2160/REF9102) was also mounted on the disk. The power supply to and signal transmission from the sensor was also established via the slip ring assembly. As before in the case of the fan noise experiments, the casing wall pressures near the rotating disk were measured with a flush mounted 1/8 in microphone (B&K 4138). The inlet nozzle was removed and a duct
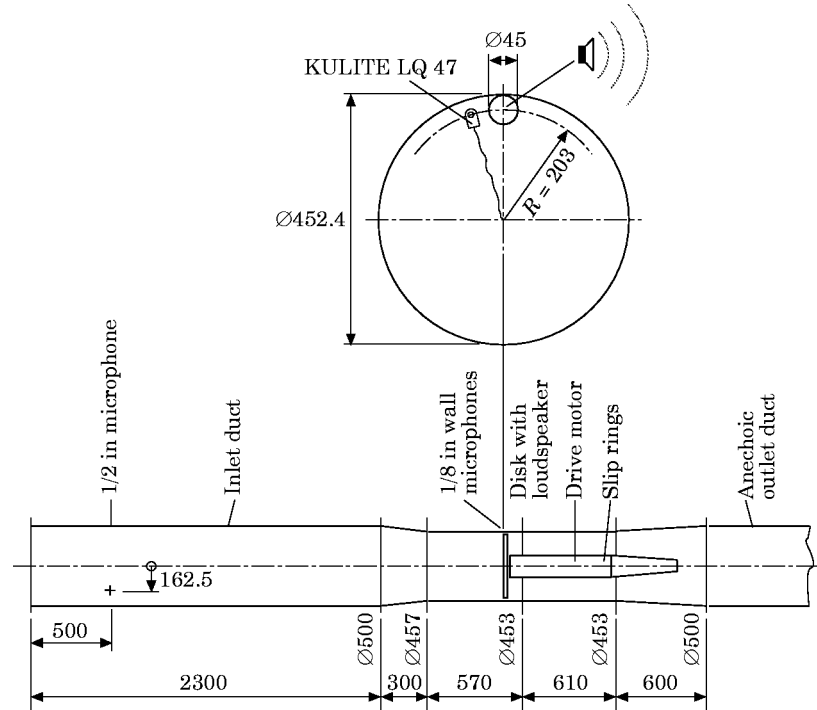

Figure 10. Schematic of the experimental setup with a rotating sound source in a duct. Dimensions in mm.

section of 2·3 m length was installed instead. A 1/2 in microphone mounted in the inlet duct at a fixed position was used to monitor the sound pressure radiated by the loudspeaker.

If the analysis of the preceding section is applied to the loudspeaker experiment, the following relations apply, upon considering that the source is locked to the rotating system:

$$\theta^Q = \theta^R, \qquad \omega^Q = \omega^R, \qquad \Omega_Q^F = \Omega, \qquad \Omega_Q^R = 0. \qquad (19, 20)$$

For this case, equations (5) and (9) become

$$\theta^Q = \theta^F - \Omega t, \qquad \omega^F = \omega^R + \alpha\Omega = \omega^R + m\Omega \qquad \text{or} \qquad f^F = f^R + mf_{shaft}. \qquad (21, 22)$$

Here the azimuthal Fourier components of the sound field (acoustic modes) are denoted by m instead of α, as customary in duct acoustics.

Figure 11(a) shows the frequency spectra measured on the rotating disk, at the duct wall near the disk (acoustic near field), and in the inlet duct (acoustic far field) for the case of a sinusoidal loudspeaker signal of 390 Hz. This frequency is just below the cut-on frequency of the first higher order azimuthal mode in the duct of 500 mm diameter, $f_{10} = 402$ Hz. The disk rotational speed was $n = 240$ r.p.m. Higher disk speeds could not be used because of mechanical vibrations. The spectrum measured by the KULITE sensor on the rotating disk is dominated by the loudspeaker signal above a random noise floor caused mainly by background noise. The two other spikes of lower level are harmonics of the mains frequency. The spectrum measured in the fixed frame of reference within the acoustic near field contains the loudspeaker signal frequency plus multiple tones at 4 Hz intervals, as predicted by equation (22) for $m = \ldots, -2, -1, 1, 2, \ldots$. These additional tones are missing in the acoustic far field spectrum, because only the plane wave component ($m = 0$) of the sound field excited by

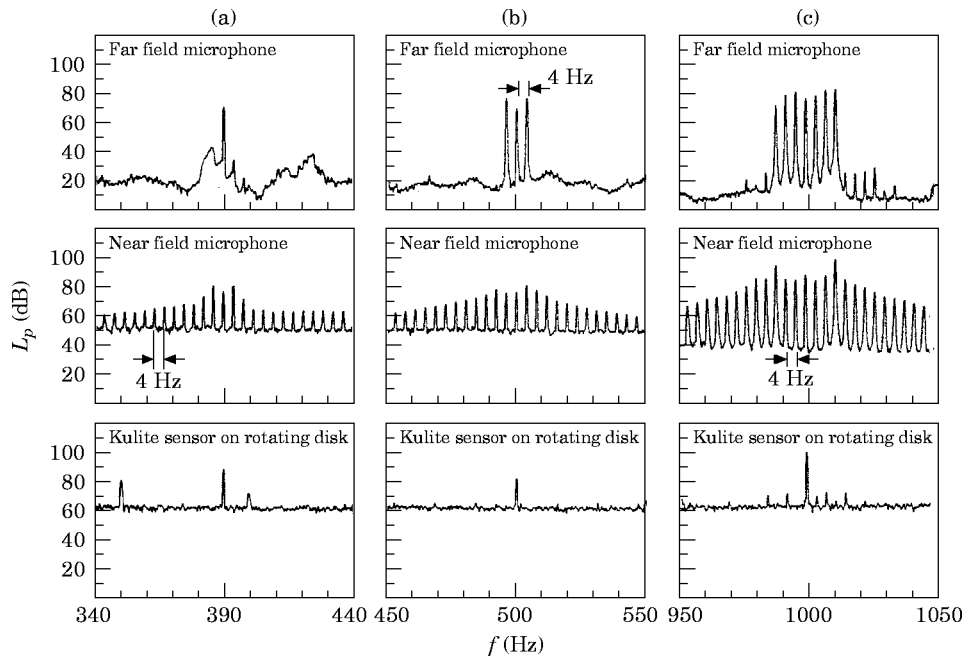

Figure 11. Sound pressure spectra generated by a rotating loudspeaker in a duct, $n = 4/s$; (a) $f^R = 390$ Hz $< f_{10}$; (b) $f^R = 500$ Hz $> f_{10}$; (c) $f^R = 1000$ Hz $> f_{30}$.

the asymmetric rotating source can propagate down the duct. The higher-order modes $m = \ldots, -2, -1, 1, 2, \ldots$ decay.

In the next experiment the frequency of the loudspeaker signal was set to 500 Hz. At this frequency the plane wave mode plus the first azimuthal mode ($m = 1$) are propagational in the test duct. Consequently, two tone components at $f = f^R \pm f_{shaft}$ are observed in the far field spectrum in addition to the source frequency f^R; compare Figure 11(b). When the loudspeaker was excited with a 1000 Hz signal, six additional tone components appeared in the far field spectrum (Figure 11(c)) due to the azimuthal modes $m = -3, -2, -1, 1, 2, 3$ which are cut-on at this frequency.

In the summary of section 5 it was noted that, due to the rotation of a fluctuating source relative to an observer, not only the source frequency ω^Q is found in the co-ordinate system of the observer but also additional tones at $\omega = \omega^Q + \alpha\Omega_Q$, where Ω_Q is the rotational speed of the source relative to the observer and $\alpha = 1, 2, 3, \ldots$ characterizes the Fourier components of the circumferentially non-uniform source distribution. Only in case of a uniform source distribution ($\alpha = 0$), is the frequency sensed by the observer equal to the original source frequency; compare equations (9) and (10).

6. INTERPRETATION OF THE ROTATING INSTABILITY COMPONENTS

In Figure 12 are depicted the spectra of the rotating instability components with enhanced frequency resolution ($\Delta f_B = 0 \cdot 125$ Hz) measured on the impeller blades, the casing wall, and in the outlet duct. The data shown are for the most efficiency point, $\Phi = 0 \cdot 22$, and two operating conditions with high levels of tip clearance noise, $\Phi = 0 \cdot 206$ and $0 \cdot 204$. For $\Phi = 0 \cdot 22$, the spectra in the entire frequency range 0–1 kHz were shown before in Figure 6 and Figure 7. In the light of the theoretical and experimental evidence presented in the previous section, the various spikes can be explained as the result of a rotating source with a non-uniform circumferential distribution. Each spike corresponds to one spatial Fourier component α (azimuthal mode number) of the source. In each spectrum, the difference between the frequencies of neighboring spikes can be interpreted as the rotational frequency of the source mechanism relative to the coordinate system considered; compare equations (15) and (16). At the best efficiency point one has, in the fixed frame of reference (casing wall pressures), when the subscript Q is replaced by RI for rotating instability, $|\Omega_{RI}^F|/2\pi = |\Delta f^F| = 10 \cdot 7$ Hz $= |\Delta\omega^F|/2\pi$, and in the rotating frame of reference (impeller blade pressures), $|\Omega_{RI}^R|/2\pi = |\Delta f^R| = 13 \cdot 1$ Hz $= |\Delta\omega^R|/2\pi$. The sum of the two frequency differences is approximately equal to the rotational frequency of the rotating frame of reference, i.e., the impeller shaft frequency: $|\Delta f_{RI}^F| + |\Delta f_{RI}^R| = 23 \cdot 8$ Hz $\cong \Omega/2\pi = 23 \cdot 33$ Hz.

Azimuthal mode orders are not given in Figure 12 for the outlet duct because only the plane wave mode $m = 0$ is propagational there below $f_{10} = 402$ Hz. Therefore the occurrence of peaks in the outlet duct spectra for $\Phi = 0 \cdot 22$ at the exact frequencies of the $m = 31, 32$, and 34 near field modes seems incidental.

Similar measurements were made at various operation conditions of the fan, and in Table 1 are listed the frequencies of the rotating instability components with the highest level, $\omega_{RI}^F/2\pi$ and $\omega_{RI}^R/2\pi$, and the rotational frequencies determined from equations (15) and (16), $\Omega_{RI}^F/2\pi$ and $\Omega_{RI}^R/2\pi$, respectively, both for the fixed and the rotating system. The magnitude of the rotational velocity of the rotating instability components normalized with the rotor angular velocity is plotted in Figure 13 as function of the flow coefficient for the tip clearance ratio $\tau = 0 \cdot 0053$.

The frequency differences between the spikes in Figure 12 can be used to determine the magnitude of the angular velocity of the rotating instability components but not its
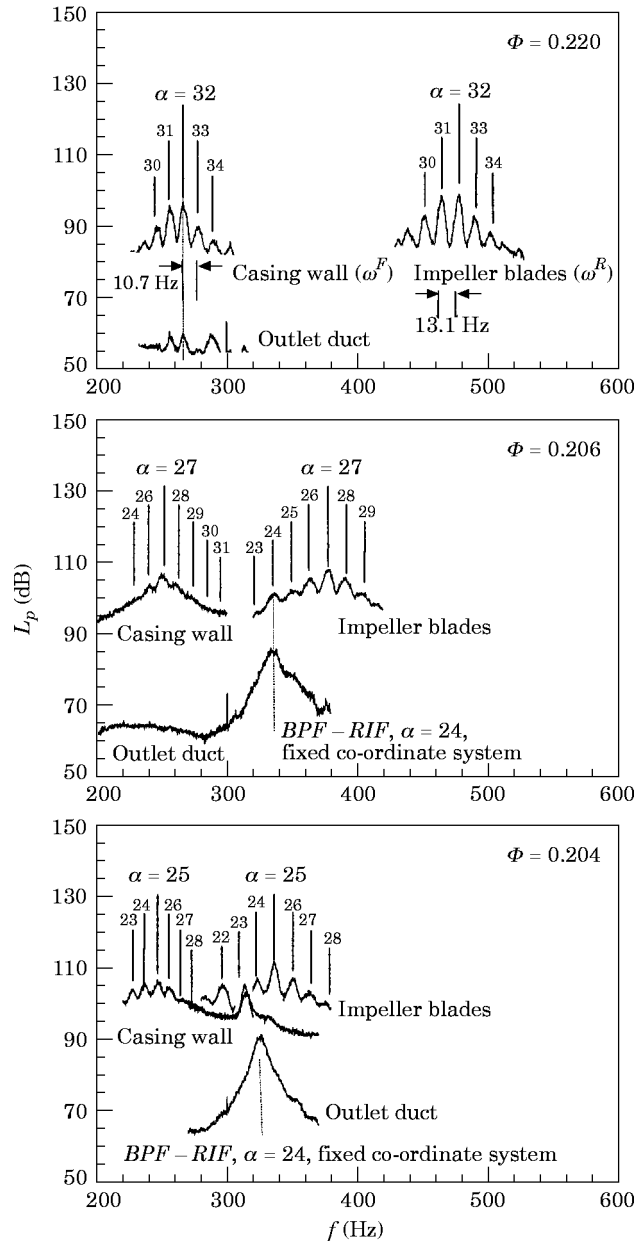
Figure 12. Pressure spectra at the casing wall (near field, $\zeta = -0.007$), in the outlet duct (far field), and on the impeller blades (sensor #2); $\tau = 0.0053$, $n = 1400$ r.p.m., $\Delta f_B = 0.125$ Hz.

direction. This is possible by considering the phase difference of the pressure signals measured at two angular locations; see for example the data shown in Figure 8. The azimuthal phase velocity a_θ of the pressure signal is equal to the angular displacement of the two measurement positions $\Delta\theta$ and the time lag Δt which in turn is given by the phase angle of the cross spectrum of the pressure signals (compare the discussion by Bendat and Pierson [19]) $\varphi_{12} = \omega\,\Delta t$. For the fixed co-ordinate system, one has

$$a_\theta^F = \Delta\theta^F/\Delta t^F = \Delta\theta^F \omega^F/\varphi_{12}^F,\tag{23}$$

TABLE 1

Frequencies, rotational velocities, and mode numbers of the rotating instability components in the fixed and the rotating co-ordinate system as functions of the fan operating condition; $\tau = 0\cdot0053$, $n = 1400$ r.p.m., $\Delta f_B = 0\cdot125$ Hz

Φ	$\dfrac{\omega^F_{RI}}{2\pi}$ (Hz)	$\dfrac{\Phi^F_{RI}}{2\pi}$ (Hz)	$\dfrac{\omega^R_{RI}}{2\pi}$ (Hz)	$\dfrac{\Omega^R_{RI}}{2\pi}$ (Hz)	$\dfrac{\omega_{CN}}{2\pi}$ (Hz)	$\dfrac{\omega^Q}{2\pi}$ (Hz)	$\alpha = \dfrac{|\omega^F_{RI}| + |\omega^R_{RI}|}{\Omega}$
0·245	252·0	8·1	518·5	−15·0	—	−15·3	33·0
0·239	251·7	8·5	541·3	−14·4	—	−37·3	34·0
0·235	259·3	9·1	534·2	−13·8	381·2	−50·1	34·0
0·228	270·7	10·1	522·1	−12·6	379·7	−72·7	34·0
0·220	267·6	10·7	479·8	−13·1	367·2	−74·8	32·0
0·215	262·7	10·1	437·2	−12·9	354·7	−40·3	30·0
0·206	251·1	10·0	378·1	−13·0	333·6	−18·6	27·0
0·204	246·5	9·8	336·6	−13·5	325·0	1·5	25·0
0·186	159·0	10·5	144·7	−12·9	—	22·3	13·0

and the corresponding relationship for the rotating system of co-ordinates is obtained by replacing the superscripts F in equation (23) by the superscript R. Equation (23) can be applied to any frequency component of the rotating instability, for example to the one with the highest coherence in the spectrum; compare Figure 8. Alternatively, the azimuthal phase velocity can be determined via the gradient of the phase angle over a range of frequencies which effectively averages the azimuthal phase velocity over that range. From equation (23) it follows that

$$a^F_\theta = 2\pi\Delta\theta^F/(\mathrm{d}\varphi^F_{12}/\mathrm{d}f), \qquad (24)$$

Equation (24) and the corresponding relationship for the rotating system of co-ordinates can be applied to the frequency range where the phase angle changes linearly with frequency; compare Figure 8. The positive slope of the phase angle in the fixed and the negative slope in the rotating frame reference reveal that the angular velocity of the rotating instability components is positive in the absolute frame of reference and negative in the rotating frame. In other words, the rotating instability components move in the same direction as the rotor but at a slower speed so that there is a relative motion between the rotating instabilities and the blade row.
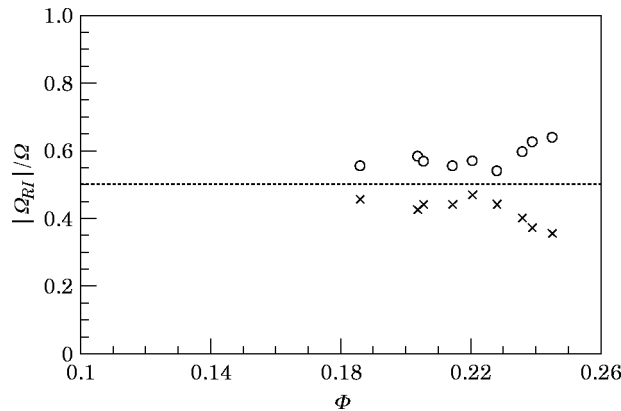

Figure 13. Normalized angular propagation velocity of the rotating instability components as a function of flow rate for the tip clearance ratio; $\tau = 0\cdot0053$; $n = 1400$ r.p.m. $\times - \times$, Fixed frame; $\bigcirc - \bigcirc$, rotating frame.

The azimuthal phase velocity can also be expressed in terms of the azimuthal wavenumber α and the angular frequency, $a_\theta = \omega/\alpha$:

$$a_\theta^F = \omega^F/\alpha = (\omega_{RI} + \alpha\Omega_{RI}^F)/\alpha = (\omega_{RI}/\alpha) + \Omega_{RI}^F, \tag{25}$$

$$a_\theta^R = \omega^R/\alpha = (\omega_{RI} + \alpha\Omega_{RI}^R)/\alpha = (\omega_{RI}/\alpha) + \Omega_{RI}^R. \tag{26}$$

Subtracting equation (26) from (25) reveals that the same relationship is valid among the azimuthal propagation velocities as for the rotational velocities in the fixed and the rotating system:

$$a_\theta^F - a_\theta^R = \Omega_{RI}^F - \Omega_{RI}^R = \Omega. \tag{27}$$

As was mentioned above, the various spikes in Figure 12 are caused by the rotation of a circumferentially non-uniform source distribution, and each spike corresponds to one particular aerodynamic mode number (or Fourier component) α. Equation (11) may be used to determine the mode number α from the frequencies measured in the fixed and the rotating frame of reference, provided one can tell which two spikes in the casing wall pressure spectrum and the impeller blade pressure spectrum belong together. This knowledge is not given *a priori*, and one therefore has to make "best guesses". A reasonable assumption is that the peaks with the highest amplitude in each spectrum correspond to one another.

Since the rotational speed of the rotating instability component as measured in the rotating co-ordinate system is negative ($\Omega_{RI}^R < 0$), two cases have to be considered in equation (10):

$$(1) \quad \omega^Q > \alpha|\Omega|, \quad \text{then} \quad \omega^R > 0; \qquad (2) \quad \omega^Q < \alpha|\Omega|, \quad \text{then} \quad \omega^R < 0.$$

Only the magnitude of the frequency can be measured by experimental equipment, and therefore equation (11) has to be modified to read

$$\alpha = (|\omega_{RI}^F| \pm |\omega_{RI}^R|)/\Omega, \tag{28}$$

where the dual sign $\pm$ reflects the two cases mentioned above. The mode number α and the source frequency ω^{RI} were calculated by inserting the peak frequencies ω_{RI}^F, ω_{RI}^R and the rotational frequency Ω_Q^F listed in Table 1 into equations (28) and (12). The results of this calculation are also given in Table 1, and in addition the mode orders are marked in Figure 12; the aerodynamic mode numbers α were obtained with the positive sign in equation (28); the negative sign yielded non-integer values which are physically meaningless.

An important observation in Figure 12 is that high levels of tip clearance noise occur at those operating conditions where the azimuthal source distribution contains mode orders equal to the number of blades, $\alpha = 24$. Note also that in these cases the frequency of the tip clearance noise is equal to the difference between blade passing frequency (*BPF*) and the rotating instability frequency (*RIF*) of the mode $\alpha = 24$. When the flow rate is reduced from $\Phi = 0{\cdot}206$ to $0{\cdot}204$, i.e., by less than 1%, the center frequency of the rotating instability component decreases significantly and the mode numbers equal to or near the blade number gain in level; however, the frequency of each mode number (e.g., $\alpha = 24$) is shifted to lower frequencies only slightly.

7. COMPARISON OF ROTATING FLOW INSTABILITY AND ROTATING STALL

The analysis presented in section 5.1. can also be applied to the case of rotating stall. This flow phenomenon occurs when a turbomachine is operated at low flow rates and some
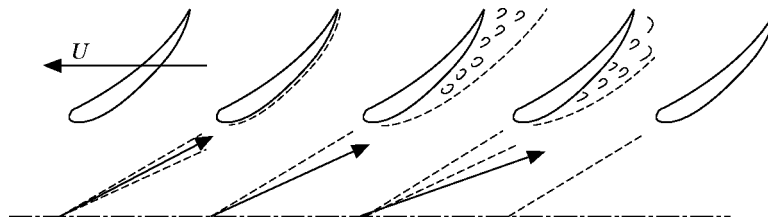
Figure 14. Schematic presentation of rotating stall in an axial flow machine.

local disturbance stalls the flow on one of the blades. A schematic of this flow condition is shown in Figure 14. As a result, the flow in the passage on the suction side of this blade is partially blocked, and the mean flow is diverted away from this passage. This in turn increases the angle of attack on the blade nearest to the suction side of the originally stalled blade so that the flow is stalled there. On the pressure side of the originally stalled blade, the flow angle is reduced, and the flow "unstalled". In this way the stall cell moves relative to the blade row; in the rotor frame of reference, the direction of rotation is opposite to that of the blades, but in the absolute frame of reference the stalled cell moves in the same direction as the rotor, at a lower speed however; see the schematic presentation in Figure 15. More than one cell of stalled flow have been observed in various experiments. It is generally understood that a rotating stall cell moves around the impeller circumference as a more or less frozen flow pattern: i.e., hardly any variation of the flow field with time occurs when moving with the cell. In the context of the theoretical considerations discussed in section 5.1. for this case the source frequency $\omega^Q = 0$, and from equations (9) and (10) it follows that, with the subscript Q replaced by RS for rotating stall,

$$\omega_{RS}^F = \alpha\Omega_{RS}^F, \qquad \omega_{RS}^R = \alpha\Omega_{RS}^R. \tag{29, 30}$$

The lowest azimuthal Fourier component α_{min} is equal to the number of stall cells. Harmonics of the fundamental stall frequency $\alpha_{min}\Omega_{RS}$ exist because the azimuthal distribution of the stall flow pattern is generally not sinusoidal. Equations (29) and (30) were used to determine the angular velocity of the rotating stall component from the pressure spectra measured on the casing wall and on the impeller blades (compare for example Figure 6 and Figure 7), and the results are shown in Figure 16 as functions of the fan operating condition and for the tip clearance ratio $\tau = 0\cdot0053$. The sum of the angular velocities in the fixed and the rotating frame of reference is equal to the impeller angular speed as prescribed by equation (4). Comparing Figure 13 and Figure 16 reveals that the angular speed of the rotating instability components is not very different from that
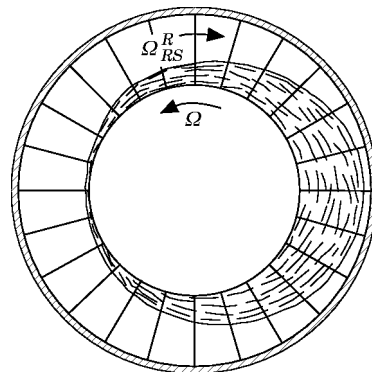

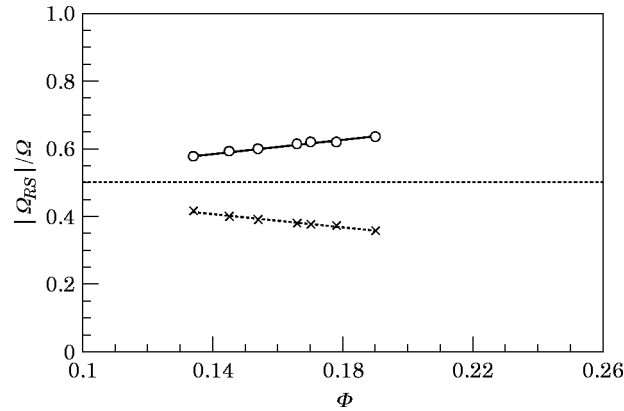Figure 15. Schematic presentation of a rotating stall cell.

Figure 16. Normalized angular velocity of the rotating stall component as function of the flow rate for the tip clearance ratio $\tau = 0 \cdot 0053$; $n = 1400$ r.p.m. $\times - \times$, Fixed frame; $\bigcirc - \bigcirc$, rotating frame.

of the rotating stall component; however the main difference between the two flow phenomena is that the rotating stall, within its own frame of reference, is a steady flow field while the rotating blade flow instability is an unsteady rotating source mechanism.

8. MODEL OF TIP CLEARANCE NOISE GENERATION

The experimental results presented above revealed that tip clearance noise is found in the acoustic far field only if the rotating blade flow instability components are present simultaneously in the near field. This phenomenon is more pronounced at the blade tip than at the hub. The analysis of the pressure spectra measured on the impeller blades and on the casing wall close to the impeller have shown that the rotating instability components can be interpreted as a source or vortex mechanism which rotates relative to the cascade at about half the impeller speed. The circumferential distribution of this rotating source is not uniform and can be represented by a superposition of spatial Fourier components, similar to the higher order azimuthal modes of sound propagation in a circular duct. Strong tip clearance noise was observed when an azimuthal mode order dominates which is equal to the number of blades: in the present case $\alpha = Z = 24$. The unsteady interaction of this flow pattern with the blade cascade is similar to the interaction of two rotors of equal blade number and different rotational speed and direction. This case was treated by Holste [20] and Holste and Neise [21]. According to these considerations, the azimuthal mode numbers and angular frequencies generated by two rotors of angular speeds Ω_1 and Ω_2 and blade numbers Z_1 and Z_2 are given by the expressions

$$m = h_1 Z_1 - h_2 Z_2, \qquad h_1, h_2 = \ldots, -1, 0, 1, \ldots, \tag{31}$$

$$\omega = h_1 Z_1 \Omega_1 - h_2 Z_2 \Omega_2, \qquad h_1, h_2 = \ldots, -1, 0, 1, \ldots. \tag{32}$$

Counter rotation is accounted for by opposite signs of the two rotor speeds.

In the case considered here, $Z_1 = Z_2 = Z = \alpha = 24$, $\Omega_1 = \Omega$, and $\Omega_2 = \Omega_{RI,\alpha = 24}$, all quantities defined in the fixed co-ordinate system, and equations (31) and (32) turn into

$$m = Z(h_1 - h_2) = \ldots, -Z, 0, Z, \ldots, \tag{33}$$

$$\omega = Z(h_1 \Omega_1 - h_2 \Omega_2) = \ldots, Z\Omega, Z\Omega_{RI,\alpha = Z}, Z(\Omega - \Omega_{RI,\alpha = Z}), Z(\Omega + \Omega_{RI,\alpha = Z}), \ldots. \tag{34}$$
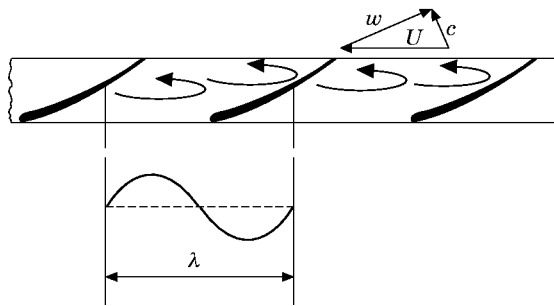
Velocity triangle at $r/R = 0.75$

Figure 17. Schematic representation of vortex separation from the blade tip. λ = blade pitch.

Most of the interaction frequencies in equation (34) can be observed in the near field (casing wall pressures) in Figure 6, Figure 8, and Figure 12. In the acoustic far field (outlet duct), only the plane wave mode $m = 0$ described by $h_1 = h_2 = h$ is found because the other modes are not propagational in the frequency range of interest here. The interaction frequencies of the plane wave mode are given by $\omega = h(Z\Omega - \Omega_{RI,\alpha = Z})$ which for $h = 1$ yields the frequency of tip clearance noise, $f_{CN} = BPF - f_{RI,\alpha = 24}$; compare the two lower diagrams in Figure 12.

The above considerations can be used to develop the following flow model. Hot wire measurements in the blade tip area and within the tip clearance gap have shown that the rotating instability only occurs if a reversed flow condition exists in the tip clearance gap (see references [1] and [2]). The rotating instability phenomenon is more pronounced at the blade tip than at the hub. If the reversed flow is strong enough to eliminate the axial component of the main flow in the blade cascade near the tip, the oncoming flow as seen by the blade tips has only an azimuthal component. As a result, vortex separation takes place at the blade tips with the vortices moving in the circumferential direction; see the flow sketch in Figure 17. If the wavelength of the shed vortices is equal to the blade spacing ($\alpha = Z$), a strong interaction of the vortex separation on individual blades occurs which results in drastic increases of the radiated noise. When the mean flow is throttled even further, flow separation takes place over the entire radial span of the blades, over part of the impeller circumference, which is the well known phenomenon of rotating stall.

9. CONCLUSIONS

An experimental study is described to investigate the aeroacoustic generation mechanism of the tip clearance noise in axial turbomachines. In the published literature higher broadband levels were reported when the tip clearance was enlarged. The present results show that in addition, significant sound pressure level increases occur within limited, almost narrow frequency bands in a region below the blade passing frequency component. This tip clearance noise component, which is a particularly effective noise source, was observed when the tip clearance ratio was larger than or equal to $\tau = s/D = 0.0027$ and if there is a high enough pressure difference between suction and pressure side of the impeller: i.e., at flow rates equal to or smaller than the design flow rate.

Measurements of the pressure fluctuations on the casing wall close to the impeller and on the rotating blades have shown that tip clearance noise is found in the acoustic far field only if the rotating blade flow instability components are present simultaneously in the near field. This phenomenon is more pronounced at the blade tip than at the hub.

The analysis of the pressure spectra measured on the impeller blades and on the casing wall close to the impeller have shown that the rotating instability components can be interpreted as a fluctuating source or vortex mechanism which rotates relative to the cascade at about half the impeller speed. The circumferential distribution of this rotating source is not uniform and can be represented by a superposition of spatial Fourier components, similar to the higher order azimuthal modes of sound propagation in circular duct.

The generation of tip clearance noise is explained by the interaction of the rotating instability component with the impeller blades. Strong tip clearance noise is observed when an azimuthal mode order dominates the rotating instability components which is equal to the number of rotor blades, $\alpha = Z$. In this case a plane sound wave is generated by the interaction and effective sound radiation into the far field occurs. The frequency and the azimuthal mode structure of the tip clearance noise component can be described by using the results of the rotor/rotor interaction analysis presented in references [20] and [21].

Hot wire measurements in the blade tip area and within the tip clearance gap (see references [1] and [2]) have shown that the rotating instability only occurs if a reversed flow condition exists in the tip clearance gap. When the reversed flow is strong enough to eliminate the axial velocity near the tips, vortex separation takes place at the blade tips with the vortices moving in the circumferential direction. If the azimuthal wavelength of the shed vortices is equal to the blade spacing ($\alpha = Z$), a strong interaction of the vortex separation on individual blades occurs which produces the tip clearance noise. When the mean flow is throttled even further, flow separation takes place over the entire radial span of the blades, over part of the impeller circumference, which is the well known phenomenon of rotating stall.

The rotating instability phenomenon discussed in this paper was also observed in the casing wall pressure fluctuations in the first stage of a multi-stage high-speed axial compressor, as was reported by Kameier and Neise [22] and Baumgartner et al. [23]. Here, the rotating blade flow instability induced blade vibrations which may be critical to mechanical stability of the machine.

REFERENCES

1. F. KAMEIER 1994 *Fortschritt Berichte VDI Reihe* 7, **243**, *Verein Deutscher Ingenieure*, *VDI Verlag GmbH*, *Düsseldorf*, *Germany* (*Doctoral Dissertation*, *Technische Universität Berlin*). Experimentelle Untersuchung zur Entstehung und Minderung des Blattspitzen-Wirbellärms axialer Strömungsmaschinen.
2. F. KAMEIER and W. NEISE 1997 (To be published). *Transactions of the ASME*, *Journal of Turbomachinery*. Experimental study of tip clearance losses and noise in axial turbomachines and their reduction.
3. H. MARCINOWSKI 1953 *Motortechnische Zeitschrift* (*MTZ*) **14**, 259–262. Einfluß des Laufradspaltes und der Luftführung bei einem Kühlgebläse axialer Bauart.
4. B. D. MUGRIDGE and C. L. MORFEY 1972 *Journal of the Acoustical Society of America* **51**, 1411–1426. Sources of noise in axial flow fans.
5. R. E. LONGHOUSE 1978 *Journal of Sound and Vibration* **58**, 201–214. Control of tip-vortex noise of axial flow fans by rotating shrouds.
6. T. FUKANO, Y. TAKAMATSU and Y. KODAMA 1986 *Journal of Sound and Vibration* **105**, 291–308. The effect of the tip clearance on the noise of low pressure axial and mixed flow fans.
7. W. STÜTZ 1988 *Strömungsmechanik und Strömungsmaschinen* **39**, 153–160 (Verlag G. Braun, Karlsruhe). Experimentelle Untersuchung zum Radialspalteinfluß auf das aerodynamische und akustische Verhalten eines Axialventilators.
8. M. CUDINA 1992 *Noise Control Engineering Journal* **39**, 21–30. Noise generated by a vane-axial fan with inlet guide vanes.

9. DIN 24 163 Teil 1–3 1985 *Deutsche Norm*, *Deutsches Institut für Normung e.V*, Berlin, Germany. Ventilatoren, Leistungsmessung.

10. DIN EN 25 136 1994 *Deutsche Norm*, *Deutsches Institut für Normung e.V*, Berlin, Germany. Bestimmung der von Ventilatoren in Kanäle abgestrahlten Schalleistung; Kanalverfahren.

11. ISO 5136 1990 *International Standard*, *International Organisation for Standardization*. Acoustics—determination of sound power radiated into a duct by fans—in-duct method.

12. J. M. TYLER and T. G. SOFRIN 1962 *Transactions of the Society of Automotive Engineers* **70**, 309–332. Axial flow compressor noise studies.

13. N. A. CUMPSTY 1977 *Transactions of the American Society of Mechanical Engineers*, *Journal of Fluids Engineering* **99**, 278–293. Review—a critical review of turbomachinery noise.

14. T. NAWROT 1992 *Diploma-thesis*; *Hermann-Föttinger-Institut für Thermo- und Fluiddynamik*, *Technische Universität Berlin*, *Germany*. Experimentelle Untersuchung zum Entstehungsmechanismus des Spitzenwirbellärms an einer axialen Strömungsmaschine.

15. F. KAMEIER, T. NAWROT and W. NEISE 1992 *Proceedings of the* 14*th DGLR/AIAA-Aeroacoustics Conference*, *Aachen*. *Paper No.: DGLR/AIAA* 92-02-040. *DGLR Bericht* **92-03**, 250–259 *Bonn*, *Germany*. Experimental investigation of tip clearance noise in axial flow machines.

16. L. MONGEAU 1991 *Ph.D. Thesis*, *The Pennsylvania State University*. Experimental study of the mechanism of sound generation by rotating stall in centrifugal turbomachines.

17. P. H. BENT, D. K. MCLAUGHLIN and D. E. THOMPSON 1992 *Proceedings of the* 14*th DGLR/AIAA-Aeroacoustics Conference*, *Aachen*, *Paper No. DGLR/AIAA* 92-02-099. *DGLR Bericht* **92-03**, 607–614, *Bonn*, *Germany*. Influence of discharge configuration on the generation of broadband noise in centrifugal turbomachinery.

18. L. MONGEAU, D. E. THOMPSON and D. K. MCLAUGHLIN 1993 *Journal of Sound and Vibration* **163**, 1–30. Sound generation by rotating stall in centrifugal turbomachines.

19. J. S. BENDAT and A. G. PIERSOL 1980 *Engineering Applications of Correlation and Spectral Analysis*. New York: John Wiley & Sons.

20. F. HOLSTE 1995 *Fortschritt Berichte VDI Reihe* 7, **272**, *Verin Deutscher Ingenieure*, *VDI Verlag GmbH*, *Düsseldorf*, *Germany* (*Doctoral Dissertation*, *Technische Universität Berlin*). Ermittlung der aerodynamischen Lärmquellen und Berechnung des abgestrahlten Schallfeldes mittels der im Nahfeld gemessenen Druckschwankungen am Beispiel eines Triebwerksmodells.

21. F. HOLSTE and W. NEISE 1995 *Proceedings of the First Joint CEAS/AIAA Aeroacoustics Conference* (16*th AIAA Aeroacoustics Conference*), *Munich*, 12–15 *June*, 1995. Paper *CEAS/AIAA*-95-178, *Deutsche Gesellschaft für Luft- und Raumfahrt—Lilienthal-Oberth e.V.* (*DGLR*) *Bonn*, *Germany*, *DGLR-Bericht* **95-01**, 1221–1229. Acoustical near field measurements on a propfan model for noise source identification.

22. F. KAMEIER and W. NEISE 1995 *Proceedings AGARD PEP* 85*th Meeting on Loss Mechanisms and Unsteady Flows in Turbomachines*. 8–12 *Mai*, *Derby*, *UK*. Reduction of tip clearance loss and tip clearance noise in axial-flow machines.

23. M. BAUMGARTNER, F. KAMEIER and J. HOURMOUZIADIS 1995 *Twelfth International Symposium on Airbreathing Engines*, *Melbourne*, *Australia*, 10–15 *September*. Non-engine order blade vibration in a high speed compressor.